



Identification of Near-infrared [Se III] and [Kr VI] Emission Lines in Planetary Nebulae*

N. C. Sterling¹, S. Madonna^{2,3}, K. Butler⁴, J. García-Rojas^{2,3}, A. L. Mashburn¹, C. Morisset⁵, V. Luridiana^{2,3}, and I. U. Roederer^{6,7}¹Department of Physics, University of West Georgia, 1601 Maple Street, Carrollton, GA 30118, USA; nsterlin@westga.edu, awhite15@my.westga.edu²Instituto de Astrofísica de Canarias, E-38205 La Laguna, Tenerife, Spain; vale@iaa.es, smadonna@iac.es, jogarcia@iac.es³Universidad de La Laguna, Dpto. Astrofísica, E-38206 La Laguna, Tenerife, Spain⁴Institut für Astronomie und Astrophysik, Scheinerstr. 1, D-81679 München, Germany; butler@usm.uni-muenchen.de⁵Instituto de Astronomía, Universidad Nacional Autónoma de México, Apdo. Postal 20164, 04510, México; chris.morisset@gmail.com⁶Department of Astronomy, University of Michigan, 1085 South University Avenue, Ann Arbor, MI 48109, USA; iur@umich.edu⁷Joint Institute for Nuclear Astrophysics and Center for the Evolution of the Elements (JINA-CEE), USA

Received 2017 January 19; accepted 2017 April 4; published 2017 May 9

Abstract

We identify [Se III] 1.0994 μm in the planetary nebula (PN) NGC 5315 and [Kr VI] 1.2330 μm in three PNe from spectra obtained with the Folded-Port InfraRed Echellette (FIRE) spectrometer on the 6.5 m Baade Telescope. Se and Kr are the two most widely detected neutron-capture elements in astrophysical nebulae, and can be enriched by *s*-process nucleosynthesis in PN progenitor stars. The detection of [Se III] 1.0994 μm is particularly valuable when paired with observations of [Se IV] 2.2864 μm , as it can be used to improve the accuracy of nebular Se abundance determinations, and allows Se ionization correction factor (ICF) schemes to be empirically tested for the first time. We present new effective collision strength calculations for Se^{2+} and Kr^{5+} , which we use to compute ionic abundances. In NGC 5315, we find that the Se abundance computed from $\text{Se}^{3+}/\text{H}^+$ is lower than that determined with ICFs that incorporate $\text{Se}^{2+}/\text{H}^+$. We compute new Kr ICFs that take $\text{Kr}^{5+}/\text{H}^+$ into account, by fitting correlations found in grids of Cloudy models between Kr ionic fractions and those of more abundant elements, and use these to derive Kr abundances in four PNe. Observations of [Se III] and [Kr VI] in a larger sample of PNe, with a range of excitation levels, are needed to rigorously test the ICF prescriptions for Se and our new Kr ICFs.

Key words: atomic data – infrared: general – nuclear reactions, nucleosynthesis, abundances – planetary nebulae: general – stars: AGB and post-AGB

Supporting material: tar.gz file

1. Introduction

Nebular spectroscopy of neutron(*n*)-capture elements (atomic number $Z > 30$) provide a valuable tool for studying slow *n*-capture nucleosynthesis (the *s*-process) in low-mass stars, revealing information independent of and complementary to spectroscopy of asymptotic giant branch (AGB) stars. In the last 15 years, this field has rapidly developed due to the discovery and detection of several *n*-capture element emission lines, predominantly in the near-infrared. Dinerstein (2001) identified two of the most widely detected trans-iron element lines in astrophysical nebulae, [Kr III] 2.1986 and [Se IV] 2.2864 μm .⁸ More recently, Sterling et al. (2016) discovered emission lines of [Rb IV], [Cd IV], and [Ge VI] in the *H*- and *K*-band spectra of two planetary nebulae (PNe).

Neutron-capture elements have been detected in more than 100 PNe in the Milky Way (Sharpee et al. 2007; Sterling & Dinerstein 2008; García-Rojas et al. 2015) and in nearby galaxies (Otsuka et al. 2011; Mashburn et al. 2016). These observations have driven efforts to determine atomic data needed to accurately derive *n*-capture element abundances (e.g., Sterling 2011; Sterling & Stancil 2011; Sterling & Witthoef 2011; Sterling et al. 2016). Detecting multiple ions of *n*-capture elements leads to more accurate abundance determinations and facilitates tests of atomic data and ionization correction factor (ICF) schemes (e.g., Sterling et al. 2015, hereafter SPD15).

In this paper, we present the first detection of [Se III] 1.0994 μm in an astrophysical nebula (the PN NGC 5315) and identify [Kr VI] 1.2330 μm in four PNe. We compute collision strengths for these ions to determine their ionic abundances. When combined with observations of [Se IV], the newly detected [Se III] feature enables more accurate nebular Se abundance determinations, and can be used to test the Se ICF formulae of SPD15 for the first time. Kr^{5+} can be populated in high-ionization objects, leaving Kr^+ (whose sole ground configuration transition at 1.8622 μm can only be detected from space) as the only significantly populated Kr ion that has not been detected in PNe.

2. Observations and Data Reduction

We observed four PNe (NGC 3918, NGC 5315, and SMP 47 and SMP 99 in the Large Magellanic Cloud (LMC)) with the Folded-Port InfraRed Echellette (FIRE) spectrograph (Simcoe et al. 2013) on the 6.5 m Baade Telescope at the Las Campanas Observatory, Chile. Each object was observed in echelle mode with a $0''.75 \times 7''$ slit for a spectral resolution $R = 4800$ over the wavelength range 0.83–2.45 μm . Details of the observations and analysis of LMC SMP 47 and SMP 99 are discussed in Mashburn et al. (2016). NGC 3918 was observed on 2013 January 22 and NGC 5315 on 2013 August 13, using on-off sequences for sky subtraction, for total on-source integration times of 1100 and 600 s, respectively. We centered the slit on the central portion of each nebula, at PA 0° for NGC 3918 and 90° for NGC 5315. For each PN, an A0V standard with a similar airmass was observed for telluric corrections and relative flux calibrations, and Th–Ar lamp spectra were used for

* This paper includes data obtained with the 6.5-m Magellan Telescopes at Las Campanas Observatory, Chile.

⁸ Vacuum wavelengths are used throughout this paper.

wavelength calibration. The data were reduced using the FIREHOSE IDL reduction pipeline.⁹ A detailed analysis of the FIRE spectrum of NGC 5315 is given in Madonna et al. (2017), and NGC 3918 will be described in a future paper.

3. Line Identifications

3.1. [Se III] 1.0994 μm

With an ionization potential range of 21.2–31.7 eV, Se^{2+} can be significantly populated in low- to moderate-excitation PNe, such as NGC 5315. Two [Se III] lines fall in the spectral range of FIRE (0.8858 and 1.0994 μm), where we use the level energies of Tauheed & Hala (2012). These correspond to the $^1\text{D}_2\text{--}^3\text{P}_1$ and $^1\text{D}_2\text{--}^3\text{P}_2$ ground configuration transitions, respectively. We detect features at both wavelengths in NGC 5315, as well as [Se IV] 2.2864 μm (Figure 1, Table 1). The 0.8858 μm line is also detected in the Ultraviolet and Visual Echelle Spectrograph (UVES) spectrum presented by Madonna et al. (2017), at higher signal-to-noise than in the FIRE data.

We identify the weak feature at 1.0992 μm as [Se III] 1.0994 μm . The radial velocity is -56 km s^{-1} , which agrees well with lines in the UVES spectrum but is slightly larger than found for other lines in the FIRE data (typically -20 to -40 km s^{-1} ; Madonna et al. 2017).

Using the Atomic Line List¹⁰, we searched for other possible identifications within $\pm 10 \text{ \AA}$ of the observed wavelength. We considered forbidden lines with excitation energies up to 10 eV and permitted lines for elements in the first three rows of the Periodic Table. No multiplet members or lines from the same upper level were found for any of the potential alternative identifications, except for He I 1.1000 μm , which is easily resolved from the 1.0992 μm feature (Figure 1). The strongest molecular transition with a similar wavelength is H_2 2–0 S(4) 1.0998 μm . However, NGC 5315 does not exhibit emission from vibrationally excited H_2 in its FIRE spectrum (Madonna et al. 2017), which makes this identification unlikely.

Therefore, [Se III] is the most probable identification for the 1.0992 μm feature. Because this line shares the same upper level as [Se III] 0.8858 μm , the relative intensities of the two lines should equal the ratio of the transition probabilities (Section 4) multiplied by the relative energies of the lines: $I(1.0994)/I(0.8858) = 1.3$. A direct comparison is complicated because the 0.8858 μm feature is contaminated by He I.

To determine the [Se III] contribution to the 0.8858 μm feature, we utilized the PySSN spectrum synthesis code (v0.2.70; D. Péquignot & C. Morisset 2017, in preparation) to remove the He I contribution. PySSN is a python version of X-SSN (D. Péquignot et al. 2012), which uses a database of transitions including relative intensities of multiplet members to generate a synthetic spectrum. It takes into account the different line profiles for various ions and emission processes, interstellar extinction, and the instrumental response. In Figure 2, we plot the PySSN synthetic H I and He I spectrum against the UVES data of Madonna et al. (2017) in the region near 0.8858 μm .¹¹ The He I contribution ($\sim 45\%$ of the measured flux) is removed in the bottom panel, and the residuals show a clear feature that corresponds to [Se III].

⁹ Available at <http://web.mit.edu/~rsimcoe/www/FIRE/>.

¹⁰ <http://www.pa.uky.edu/~peter/newpage/>

¹¹ The PySSN fit is in air wavelengths, since the v0.2.70 transition database utilizes only air wavelengths in the optical and *I* band.

Correcting for the He I contribution results in $I(1.0994)/I(0.8858) = 2.0 \pm 1.3$. This is somewhat larger than predicted, and is likely due to the uncertain correction for He I to the weak 0.8858 μm line. Nevertheless, the observed and expected ratios agree within the uncertainties, which supports our identification.

3.2. [Kr VI] 1.2330 μm

In the FIRE spectra of NGC 3918 and the LMC PNe SMP 47 and SMP 99, we detect a line at 1.2330 μm (rest wavelength) that we identify as [Kr VI] 1.2330 μm . This is the only collisionally excited transition of Kr^{5+} , whose ground configuration has a single ^2P term. Kr^{5+} has an ionization potential range of 64.7–78.5 eV, and thus is detectable in high-ionization nebulae such as these three objects.

There are several possible identifications for the 1.2330 μm feature, most notably H_2 3–1 S(1) 1.2330, [Fe VI] 1.2330, and N I 1.2329 μm (see below). For each of the observed PNe, we did not detect multiplet members or lines from the same upper level for any atomic transitions within 10 \AA of the observed wavelength. SMP 47 exhibits vibrationally excited H_2 emission that is consistent with fluorescent excitation in a moderate density gas (Mashburn et al. 2016), and H_2 likely contributes to the 1.2330 μm feature in this PN. According to model 14 of Black & van Dishoeck (1987), the H_2 3–1 S(1) line is 1.9 times stronger than 3–1 S(2) 1.2076 μm , and accounts for approximately 50% of the 1.2330 μm flux in SMP 47. In Figure 3, we show a PySSN fit of the H_2 contribution to the 1.2330 μm feature in SMP 47, set to $1.9F$ (H_2 3–1 S(2)). The bottom panel shows the residual emission due to [Kr VI]. NGC 3918 and SMP 99 do not exhibit vibrationally excited H_2 emission, and no correction is needed for those PNe.

A feature at 1.2330 μm was previously detected in other objects, but is likely due to [Kr VI] only in the PN NGC 7027 (Rudy et al. 1992; Kelly & Latter 1995, Table 1). In low-excitation objects, such as Hb 12, BD+30°3639, M 1–11, and the Orion nebula (Kelly & Latter 1995; Hora et al. 1999; Otsuka et al. 2013), the intensity of 1.2330 μm relative to other H_2 lines indicates that it can be identified as H_2 3–1 S(1). The detection of [Fe VI] lines in the *J*-band spectra of classical novae (e.g., Lynch et al. 2001; Rudy et al. 2002), including multiplet members of [Fe VI] 1.2330 μm , suggests that the 1.2330 μm line in these objects can be attributed to [Fe VI]. In the low-excitation PN SMC Lin 49 (Otsuka et al. 2016), the line is likely due to N I 1.2329 μm based on the detection of both multiplet members. These examples illustrate the need for caution when identifying the 1.2330 μm feature as [Kr VI].

4. Collision Strength Calculations

The collisional data for Se^{2+} and Kr^{5+} were calculated using the R-matrix method (Berrington et al. 1995). Relativistic effects (mass, velocity, and Darwin terms) were included using the intermediate-coupling frame transformation method (Griffin et al. 1998). The radial scaling parameters for the target ion and the scattering target were obtained in the configuration interaction approximation with AUTOSTRUCTURE (Badnell 2011).

Details and results of the calculations are given in Tables 2 and 3. We utilized kappa-averaged relativistic wavefunctions,

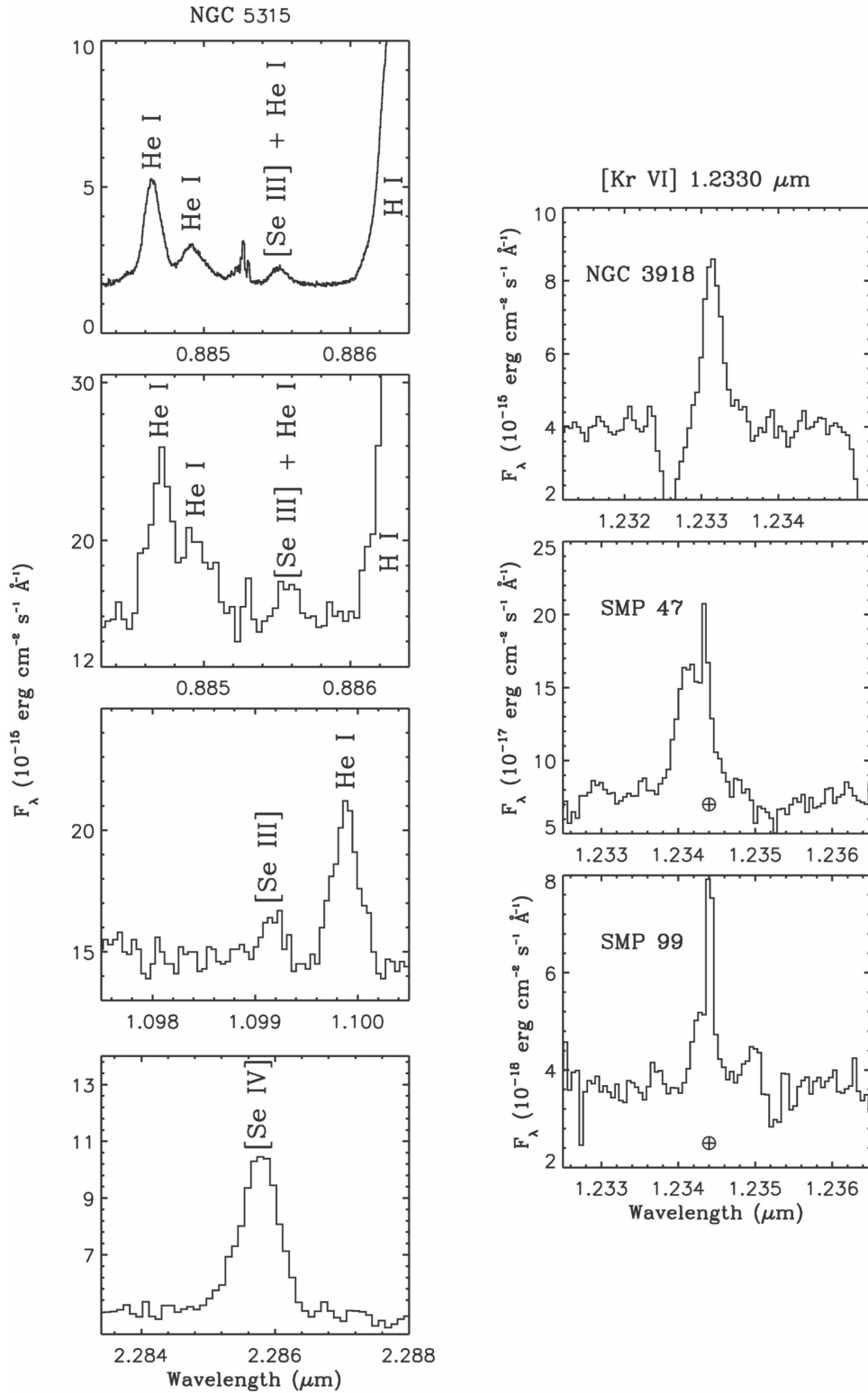


Figure 1. Left panels: [Se III] and [Se IV] detections in the UVES (top panel; Madonna et al. 2017) and FIRE spectra of NGC 5315. Right panels: [Kr VI] 1.2330 μm detections in NGC 3918, and the LMC PNe SMP 47 and SMP 99. Telluric lines (removed by Gaussian fits in the flux measurements) are indicated by ⊕ symbols.

which give markedly better energy levels and transition probabilities for these ions, although they have little effect on the collisional data. The lambda parameters scale a Thomas–Fermi–Dirac–Almadi potential for each of the electron orbitals, and were determined using a two-step process. First, the $1s$ through $4p$ scaling parameters were determined by minimizing

the energies of LS terms in the ground configuration of each ion, and then these scaling parameters were fixed when computing those for other orbitals on the first 23 (Se $^{2+}$) and 24 (Kr $^{5+}$) target term energies. The calculated energies are in excellent agreement (9% or better) with observed values from the National Institute of Standards and Technology (NIST;

Table 1
Se and Kr Intensities and Abundances

PN Name	Ion	λ (μm)	$I(\lambda)/I(\text{H I})^a$ $\times 100$	$I(\lambda)/I(\text{H I})_{\text{corr}}^b$ $\times 100$	X^{+i}/H^+ $\times 10^{-9}$	ICF	12+ Log(X/H)	12+ Log(X/H) _{Lit}
NGC 5315	[Se III]	0.8858 ^c	0.18 ± 0.05	0.10 ± 0.05	1.3 ± 0.7	3.6 ± 2.8	3.67 ± 0.45	...
	[Se III]	0.8858	0.20 ± 0.07	0.11 ± 0.07	1.5 ± 0.8		3.72 ± 0.45	
	[Se III]	1.0994	0.21 ± 0.07	...	2.1 ± 0.8		3.89 ± 0.27	
	[Se IV]	2.2864	2.95 ± 0.32	...	0.80 ± 0.08	1.7 ± 0.5	3.12 ± 0.13	
NGC 3918	[Kr VI]	1.2330	0.44 ± 0.06	...	0.18 ± 0.03	1.3 ± 0.5^d	3.70 ± 0.21^d	
						5.1 ± 0.1	2.95 ± 0.08	3.97 ± 0.12
LMC SMP 47	[Kr VI]	1.2330	0.46 ± 0.06	0.22 ± 0.11	0.08 ± 0.06	7.8 ± 3.2	2.82 ± 0.39	3.75 ± 0.20
LMC SMP 99	[Kr VI]	1.2330	0.21 ± 0.04	...	0.11 ± 0.03	36 ± 21	3.59 ± 0.34	3.78 ± 0.21
NGC 7027 ^f	[Kr VI]	1.2330	1.1 ± 0.3	1.0 ± 0.3	0.53 ± 0.16	5.0 ± 2.6	3.42 ± 0.24	4.01 ± 0.10
						1.2 ± 0.1^e	4.10 ± 0.04^e	

Notes. Intensities and ionic and elemental abundances, are given for each Se line in NGC 5315, using the ICF schemes of SPD15: Equation (7) for [Se III] lines and Equation (8) for [Se IV]. Elemental Kr abundances were derived from $\text{Kr}^{5+}/\text{H}^+$, using Equation (1) (Section 5.2). Kr abundances from the literature (the last column) are from García-Rojas et al. (2015) for NGC 3918, Mashburn et al. (2016) for the LMC PNe, and SPD15 for NGC 7027.

^a We use H I Pa δ as the reference line for [Se III], Br γ for [Se IV], and Pa β for [Kr VI].

^b [Se III] 0.8858 μm intensity corrected for contamination by He I 0.8857 μm , and [Kr VI] 1.2330 μm intensities corrected (if necessary) for H₂ 3-1 S(1) 1.2330 μm . The error bars account for uncertainties in the deblending procedure.

^c Intensity from UVES data (Madonna et al. 2017).

^d Elemental Se abundance computed from $(\text{Se}^{2+} + \text{Se}^{3+})/\text{H}^+$, using Equation (9) of SPD15 and $\text{Se}^{2+}/\text{H}^+$ from the 1.0994 μm line.

^e Elemental Kr abundance computed from Equation (2) (Section 5.2), using the Kr^{2+} - Kr^{4+} ionic abundances from García-Rojas et al. (2015) for NGC 3918 and Sharpee et al. (2007) for NGC 7027.

^f Intensity from Kelly & Latter (1995), with an assumed uncertainty of 30%.

Kramida et al. 2016).¹² Our Se^{2+} transition probabilities agree with those of Biémont & Hansen (1986) to within 15% or better, with the exception of the weak E2 transition $^1\text{D}_2$ - $^3\text{P}_0$ (60%), and a similar agreement is found for Kr^{5+} with Biémont & Hansen (1987).

The scattering calculations for Se^{2+} included 23 target terms, which led to a 41-level calculation once relativistic effects were included. The corresponding numbers for Kr^{5+} are 24 and 52. The calculated term and level energies were replaced by NIST values when available. We described the scattered electrons with 44 and 39 continuum orbitals for the respective ions. The collision strengths were calculated with the UK-APAP codes¹³ (Badnell 1999), using fixed energy grids with $10^{-5}z^2$ Ryd steps, where z is the ion charge, to resolve resonance structures at low energies, and a coarser mesh of $0.01z^2$ Ryd at higher energies where the collision strengths are smooth. The R-matrix calculations included exchange up to $L = 12$ (corresponding to $J = 9.5$ and 10 for Se^{2+} and Kr^{5+}), and were “topped up” with non-exchange data up to $J = 37.5$ and 38 . The sum over J was completed by extrapolation procedures involving the Born approximation and geometric sums (e.g., Witthoef et al. 2006). The resulting total collision strengths were convolved with a Maxwellian distribution for a number of temperatures to produce the effective collision strengths $\Upsilon(T)$ in Table 3. Downward collisional rate coefficients q_{ji} from level j to level i can be computed via

$$q_{ji} = \frac{8.631 \times 10^{-6}}{T^{1/2}g_j} \Upsilon(T),$$

where g_j is the statistical weight of the upper state. Based on the agreement of the energy levels and the transition probabilities,

we estimate that the error bars on the collision strengths are no larger than $\sim 30\%$.

5. Results and Discussion

We computed ionic Se abundances in NGC 5315 and $\text{Kr}^{5+}/\text{H}^+$ in the other PNe (Table 1), including NGC 7027 using the data of Kelly & Latter (1995). The abundances were derived with PyNeb (Luridiana et al. 2015), using the transition probabilities and effective collision strengths from Table 3 and Se^{3+} atomic data from Biémont & Hansen (1987) and K. Butler (2007, private communication). We adopt electron temperatures and densities from Madonna et al. (2017) for NGC 5315, Leisy & Dennefeld (2006) for the Large Magellanic Cloud (LMC) PNe, García-Rojas et al. (2015) for NGC 3918, and Sharpee et al. (2007) for NGC 7027. The error bars for the ionic abundances account for uncertainties in line fluxes, temperatures, and densities, which were propagated via Monte Carlo simulations.

5.1. The Se Abundance in NGC 5315

Se^{2+} is the only Se ion other than Se^{3+} that has been detected in PNe. The detection of the uncontaminated [Se III] 1.0994 μm line (0.8858 μm is often blended with a He I line) allows nebular Se abundances to be determined more accurately than previously possible. This feature can also be used to compute Se abundances in low-ionization nebulae in which [Se IV] is not detected. In addition, this detection enables the ICF formulae of SPD15 to be empirically tested for the first time. Such tests are critical for verifying the accuracy of atomic data governing the ionization balance, as illustrated for the case of Kr by SPD15. The Se ICFs from SPD15 are:

¹² <http://physics.nist.gov/asd>

¹³ http://amdpp.phys.strath.ac.uk/UK_RmaX/codes.html

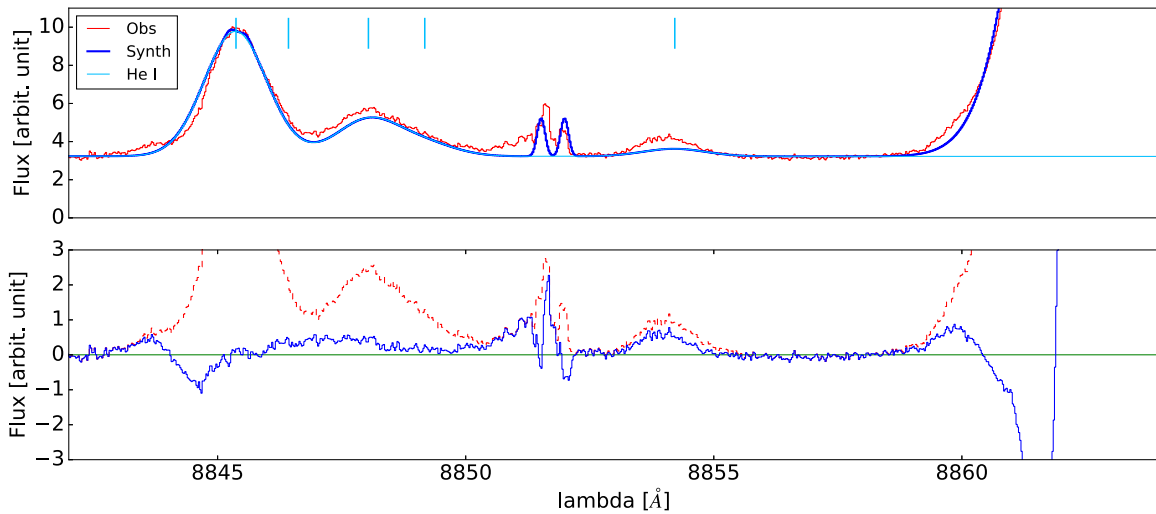


Figure 2. PySSN fit to the NGC 5315 spectrum near [Se III], with flux in arbitrary units and wavelengths in Å. The top panel compares the synthetic H I and He I spectrum (blue line) to the observed UVES spectrum of Madonna et al. (2017). In the bottom panel, the residuals of the fit (blue line) are plotted against the observed spectrum (red dashed line). A feature near $0.8854 \mu\text{m}$ is visible in the residuals, which corresponds to [Se III].

Equation (7)

$$\begin{aligned} \text{ICF}(\text{Se}) &= \text{Se}/\text{Se}^{2+} = (2.411 + 0.5146x^{12.29} \\ &\quad - 2.417e^{-0.1723x})^{-1}, \\ x &= \text{Ar}^{2+}/\text{Ar} \geq 0.0344; \end{aligned}$$

Equation (8)

$$\begin{aligned} \text{ICF}(\text{Se}) &= \text{Se}/\text{Se}^{3+} = (0.03238 + 0.3225x + 0.4013x^2)^{-1}, \\ x &= \text{O}^{2+}/\text{O}; \end{aligned}$$

Equation (9)

$$\begin{aligned} \text{ICF}(\text{Se}) &= \text{Se}/(\text{Se}^{2+} + \text{Se}^{3+}) \\ &= (-0.3703 + 0.3558e^{1.27x})^{-1}, \\ x &= (\text{Cl}^{2+} + \text{Cl}^{3+})/\text{Cl} \geq 0.0315. \end{aligned}$$

We retain the equation numbering of SPD15 to avoid confusion. Below the lower limits to x for Equations (7) and (9), the ICFs are negative and thus invalid. Equation (9) is expected to be the most accurate ICF, as it accounts for both Se^{2+} and Se^{3+} , which reduces the magnitude and importance of uncertainties in the correction for unobserved ions.

Most nebular Se abundances have been derived with Equation (8), since Se^{3+} has thus far been the only Se ion unambiguously detected in most PNe. Using this ICF, SPD15 and Mashburn et al. (2016) found that some PNe that exhibit s -process enhancements of Kr are not enriched in Se; in some cases, the Se abundance relative to O or Ar is subsolar. In Galactic PNe exhibiting both Se and Kr emission, $[\text{Kr}/\text{Se}] = 0.5 \pm 0.2$ (SPD15), which is larger than the values of 0.1–0.2 dex predicted by recent AGB nucleosynthesis models (e.g., Cristallo et al. 2015; Karakas & Lugaro 2016). The discrepancy with models raises the question of whether Equation (8) underestimates elemental Se abundances, or if the difference can be attributed to observational uncertainties.

Values for the Se abundance in NGC 5315, derived with Equations (7)–(9), are given in Table 1. Due to the uncertainty

of the [Se III] $0.8858 \mu\text{m}$ flux after correcting for He I contamination, we utilize only the $1.0994 \mu\text{m}$ line for the $\text{Se}^{2+}/\text{H}^+$ abundance. Interestingly, Equations (7) and (9) give larger Se abundances in NGC 5315 than Equation (8). The Se abundance from Equation (9) combined with $[\text{Kr}/\text{H}]$ from Madonna et al. (2017) gives $[\text{Kr}/\text{Se}] = -0.10 \pm 0.22$. In contrast, the Se abundance is subsolar if derived using Equation (8), resulting in $[\text{Kr}/\text{Se}] = 0.48 \pm 0.15$.

However, conclusions regarding the accuracy of the Se ICFs should not be drawn from a single PN. The discrepancy in the Se abundances from different ICFs may be due to observational uncertainties, inaccuracies in the atomic data governing the ionization balance of Se, or a breakdown of Equation (8) in PNe with excitation levels similar to NGC 5315 (as seen for the Kr ICF Equation (3) of SPD15). Observations of [Se III] $1.0994 \mu\text{m}$ in additional PNe, with a range of excitation levels, are needed to fully test the Se ICFs of SPD15.

5.2. Kr^{5+} Abundances and New Kr ICFs

The detection of [Kr VI] enables more accurate nebular Kr abundance determinations, although the effect is not as large as that of [Se III] on Se abundances due to the relatively small Kr^{5+} fractional abundance. In the PNe we consider, the Kr^{5+} abundance is 2–20 times smaller than Kr^{2+} and/or Kr^{3+} (Sharpee et al. 2007; García-Rojas et al. 2015; Mashburn et al. 2016), the two most dominant Kr ions in PNe.

To compute elemental Kr abundances from the [Kr VI] $1.2330 \mu\text{m}$ line, we searched for correlations between Kr^{5+} ionic fractions (and combinations of Kr ions including Kr^{5+}) and those of commonly detected lighter species in the grids of Cloudy (Ferland et al. 2013) models of SPD15. The strongest correlations are depicted in Figure 4. The Kr^{5+} fractional abundance is correlated with that of He^{2+} , albeit with a relatively large dispersion that increases for grids that include dust or have subsolar metallicities. No other significant correlations were found for Kr^{5+} , and thus the ICF to convert $\text{Kr}^{5+}/\text{H}^+$ to elemental Kr/H abundances is uncertain. In contrast, the fraction of all detected Kr ions in PNe ($\text{Kr}^{2+} - \text{Kr}^{5+}$) shows a tighter correlation with the O^{2+}/O^+ ratio.

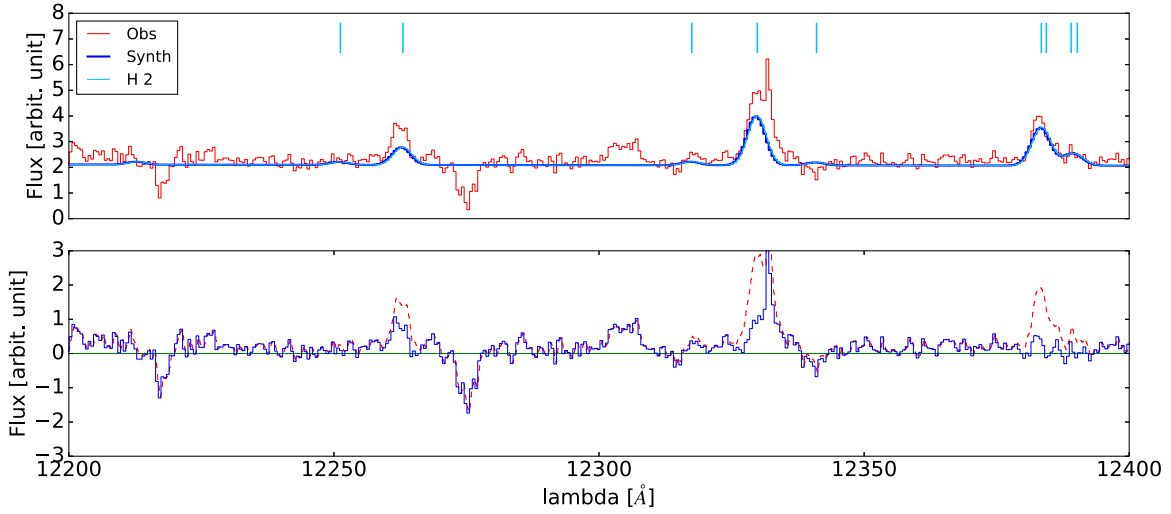


Figure 3. PySSN fit to the SMP 47 spectrum near [Kr VI] 1.2330 μm , with flux in arbitrary units and vacuum wavelengths corrected for the systemic velocity of the nebula. The top panel compares the synthetic H₂ spectrum (blue line, with wavelengths from Abgrall et al. 2000) to the observed spectrum, with line strengths scaled to H₂ 3-1 S(2) 1.2076 μm using the relative intensities from model 14 of Black & van Dishoeck (1987). Note that [Fe II] 1.2304 μm is not included in the synthetic fit. In the bottom panel, the residuals of the fit (blue line) show an emission feature at 1.2330 μm , which we identify as [Kr VI].

Table 2
Comparison of Calculated and Experimental Energies

Config.	Level	Energy (NIST, cm^{-1})	Energy (cm^{-1})	Diff. (%)
Se^{2+a}				
4s ² 4p ²	³ P ₀	0	0	...
	³ P ₁	1741	1700	-2.4
	³ P ₂	3937	3914	-0.6
	¹ D ₂	13032	14211	9.0
	¹ S ₀	28430	29985	5.5
4s4p ³	⁵ S ₂	...	61473	...
	³ D ₁	91091	89796	-1.4
	³ D ₂	92723	89868	-3.1
	³ D ₃	96548	90346	-6.4
	³ P ₀	106482	104358	-2.0
	³ P ₂	106515	104543	-1.9
	³ P ₁	106591	104579	-1.9
Kr^{5+b}				
4s ² 4p	² P _{1/2}	0	0	...
	² P _{3/2}	8110	7774	-4.3
4s4p ²	⁴ P _{1/2}	107836	104288	-3.4
	⁴ P _{3/2}	111193	107442	-3.5
	⁴ P _{3/2}	115479	111589	-3.5
	² D _{5/2}	141672	140206	-1.0
	² D _{3/2}	142727	141068	-1.2
	² S _{5/2}	170084	172042	1.1
	² P _{1/2}	180339	184060	2.0
	² P _{1/2}	183817	187921	2.1

Notes.

^a The configuration expansion for Se²⁺ is: 4s²4p², 4s4p³, 4s²4p4d, 4s²4d², 4s4p²4d, 4s4p4d², 4p⁴, 4p³4d, 4p²4d², 4s²4p4f, 4s²4p5s, 4s²4p5p, 4s4p²4f, 4s4p²5s, 4s4p²5p, 4p³4f, 4p³5s, 4p³4f, 4p³5p. The scaling parameters used are 1.42629 (1s), 1.14035 (2s), 1.08559 (2p), 1.03542 (3s), 1.01549 (3p), 0.99471 (3d), 0.96839 (4s), 0.97685 (4p), 1.01920 (4d), 1.41658 (4f), 0.98618 (5s), and 0.98063 (5p).

^b The configuration expansion for Kr⁵⁺ includes all 46 one- and two-electron promotions from the ground configuration 4s²4p into the 4p, 4d, 4f, 5s, 5p, and 5d orbitals. The scaling parameters, listed in the same order as those for Se²⁺, are 1.42203, 1.13758, 1.08300, 1.03631, 1.01532, 0.99812, 0.98673, 0.98961, 1.00041, 1.07879, 1.01934, 1.01568, and 1.01620 (5d).

We fit each correlation with an analytic function, the inverse of which serves as an ICF:

$$\text{ICF}(\text{Kr}) = \text{Kr}/\text{Kr}^{5+} = (2.881 \times 10^{-5} - 16.58x^{7.215} + 474.1x^{4.974}e^{-7.84x})^{-1},$$

$$x = \text{He}^{2+}/\text{He}; \quad (1)$$

and

$$\text{ICF}(\text{Kr}) = \text{Kr}/(\text{Kr}^{2+} + \text{Kr}^{3+} + \text{Kr}^{4+} + \text{Kr}^{5+})$$

$$= (-1206.83 + 1207.62x^{3.568 \times 10^{-5}} - 0.6035e^{-0.4583x})^{-1},$$

$$x = \text{O}^{2+}/\text{O}^{+} \geq 0.01671. \quad (2)$$

In Equation (2), the ICF is negative for O²⁺/O⁺ values below the denoted limit.

Equation (2), which primarily corrects for Kr⁺, produces Kr abundances that agree well with results from the literature (Table 1). Equation (1) tends to underestimate the Kr abundance compared to other ICFs, and shows a possible trend with nebular excitation. The Kr abundance derived with this equation agrees within the uncertainties with other estimates in SMP 99 (Mashburn et al. 2016), which has He²⁺/He = 0.19 (Leisy & Dennefeld 2006), but is lower than previous estimates by factors of 4–10 for the other more highly excited PNe (He²⁺/He \approx 0.3–0.4; Zhang et al. 2005; Leisy & Dennefeld 2006; García-Rojas et al. 2015). This poor accuracy is perhaps unsurprising given that the small Kr⁵⁺ ionic fractions and the uncertainties of the ICFs derived from Equation (1). Observations of [Kr VI] in additional PNe, paired with deep optical spectra in which other Kr ions are detected, are needed to fully test the accuracy of Equation (1) and determine whether the discrepancies with other ICFs can be attributed to observational uncertainties or the ICF itself.

6. Conclusions

The detections of [Se III] 1.0994 and [Kr VI] 1.2330 μm provide the means to improve the accuracy of nebular Kr and

Table 3
Se²⁺ and Kr⁵⁺ Transition Probabilities and Effective Collision Strengths

Trans.	A_{ij} (s ⁻¹)	Effective Collision Strength $\Upsilon(T)$										
		2000 K	4000 K	6000 K	8000 K	10,000 K	12,000 K	14,000 K	16,000 K	18,000 K	20,000 K	50,000 K
Se ²⁺												
³ P ₁ - ³ P ₀	8.708E-02	1.83	1.80	1.77	1.76	1.76	1.77	1.78	1.78	1.79	1.79	1.76
³ P ₂ - ³ P ₀	1.693E-04	1.14	1.10	1.10	1.11	1.13	1.15	1.18	1.21	1.24	1.27	1.46
³ P ₂ - ³ P ₁	1.418E-01	4.60	4.46	4.49	4.55	4.62	4.70	4.78	4.87	4.94	5.02	5.47
¹ D ₂ - ³ P ₀	3.821E-04	6.48E-01	6.54E-01	6.46E-01	6.44E-01	6.48E-01	6.57E-01	6.68E-01	6.79E-01	6.90E-01	7.01E-01	7.67E-01
¹ D ₂ - ³ P ₁	8.076E-01	2.04	2.08	2.06	2.07	2.08	2.11	2.15	2.18	2.22	2.25	2.43
¹ D ₂ - ³ P ₂	1.310	3.85	3.92	3.92	3.93	3.96	4.00	4.04	4.09	4.13	4.18	4.34
¹ S ₀ - ³ P ₀	...	1.43E-01	1.37E-01	1.39E-01	1.45E-01	1.51E-01	1.57E-01	1.62E-01	1.66E-01	1.70E-01	1.73E-01	1.78E-01
¹ S ₀ - ³ P ₁	1.756E+01	4.19E-01	4.01E-01	4.03E-01	4.18E-01	4.36E-01	4.52E-01	4.65E-01	4.75E-01	4.83E-01	4.89E-01	4.81E-01
¹ S ₀ - ³ P ₂	5.108E-01	7.21E-01	6.79E-01	6.76E-01	6.97E-01	7.24E-01	7.49E-01	7.71E-01	7.88E-01	8.01E-01	8.11E-01	7.92E-01
¹ S ₀ - ¹ D ₂	3.380	2.16	1.85	1.75	1.74	1.77	1.82	1.88	1.94	1.99	2.05	2.42
Kr ⁵⁺												
² P _{3/2} - ² P _{1/2}	4.229	1.11E+01	1.22E+01	1.25E+01	1.25E+01	1.23E+01	1.21E+01	1.19E+01	1.17E+01	1.15E+01	1.13E+01	9.71

Note. The full collision strength results and radiative data in the adf04 format of the ADAS project (<http://www.adas.ac.uk/man/appxa-04.pdf>) are available as supplementary data files to this article.

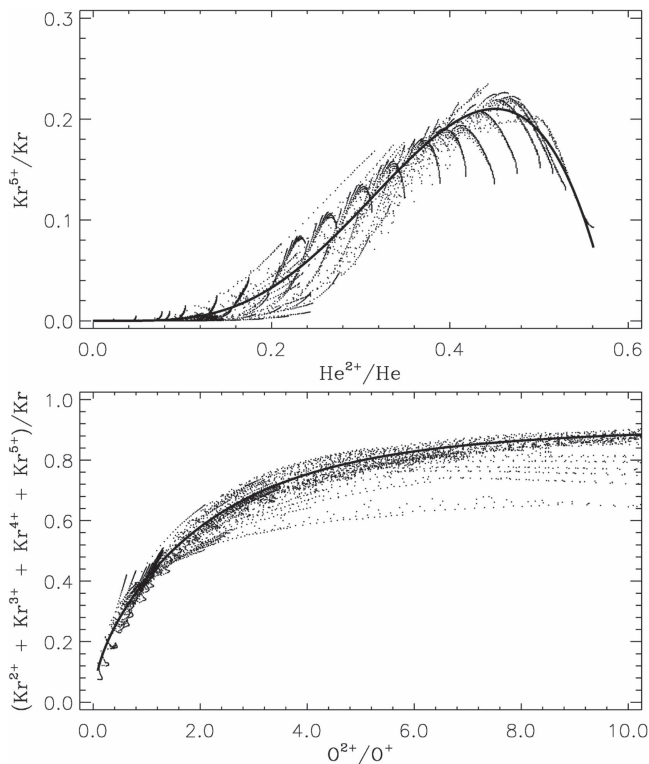


Figure 4. Correlations between the fractional abundances of Kr^{5+} and He^{2+} (top panel) and the sum of detected Kr ions and the $\text{O}^{2+}/\text{O}^{+}$ ratio, from SPD15’s grid of Cloudy models. The correlations shown are for the Cloudy “default” PN abundances (C-rich) without dust grains, with each dot representing a single model out of 10,471 in the grid. Similar correlations are found for other grids. The thick solid lines represent the analytical fits to the correlations given in Equations (1) and (2).

especially Se abundances. These are the most widely detected n -capture elements in astrophysical nebulae, and have been used to study s -process enrichments in numerous PNe. We compute collision strengths for each ion and use these to derive ionic abundances. We test the Se ICF prescriptions of SPD15, and find a larger Se abundance in NGC 5315 with ICFs that include $\text{Se}^{2+}/\text{H}^{+}$ than the ICF that relies only on $\text{Se}^{3+}/\text{H}^{+}$. We also derive Kr ICFs that incorporate $\text{Kr}^{5+}/\text{H}^{+}$ abundances, and apply these to four PNe. Additional observations of these lines in PNe with a range of excitation levels are needed to more rigorously test the Se ICFs of SPD15 and our new Kr ICFs.

We thank A. Karakas for discussions of Kr/Se ratios produced by s -process nucleosynthesis. N.C.S. acknowledges support from NSF award AST-0901432, I.U.R. from NSF grant PHY 14-30152 (Physics Frontier Center/JINA-CEE), and J.G.-R. and S.M. from the Spanish Ministry of Economy

and Competitiveness (MINECO) grant AYA2015-65205-P and Severo Ochoa Program SEV-2015-0548. S.M. acknowledges a Ph.D. fellowship from Instituto de Astrofísica de Canarias, and a Universidad de La Laguna travel grant supporting a visit to the University of West Georgia, where part of this work was done. This work has made use of NASA’s Astrophysics Data System.

References

- Abgrall, H., Roueff, E., & Drira, I. 2000, *A&AS*, **141**, 297
 Badnell, N. R. 1999, *JPhB*, **32**, 5583
 Badnell, N. R. 2011, *CoPhC*, **182**, 1528
 Berrington, K. A., Eissner, W. B., & Norrington, P. H. 1995, *CoPhC*, **92**, 290
 Biémont, E., & Hansen, J. E. 1986, *PhysS*, **33**, 117
 Biémont, E., & Hansen, J. E. 1987, *NIMPB*, **23**, 274
 Black, J. H., & van Dishoeck, E. F. 1987, *ApJ*, **322**, 412
 Cristallo, S., Straniero, O., Piersanti, L., & Gobrecht, D. 2015, *ApJS*, **219**, 40
 Dinerstein, H. L. 2001, *ApJL*, **550**, L223
 Ferland, G. J., Porter, R. L., van Hoof, P. A. M., et al. 2013, *RMxAA*, **49**, 137
 García-Rojas, J., Madonna, S., Luridiana, V., et al. 2015, *MNRAS*, **452**, 2606
 Griffin, D. C., Badnell, N. R., & Pindzola, M. S. 1998, *JPhB*, **31**, 3713
 Hora, J. L., Latter, W. B., & Deutsch, L. K. 1999, *ApJS*, **124**, 195
 Karakas, A. I., & Lugaro, M. 2016, *ApJ*, **825**, 26
 Kelly, D. M., & Latter, W. B. 1995, *AJ*, **109**, 1320
 Kramida, A., Ralchenko, Yu., Kramida, A. E., Reader, J. & NIST ASD Team 2016, NIST Atomic Spectra Database v. 5.4 (Gaithersburg, MD: NIST)
 Leisy, P., & Dennefeld, M. 2006, *A&A*, **456**, 451
 Luridiana, V., Morisset, C., & Shaw, R. A. 2015, *A&A*, **573**, 42
 Lynch, D. K., Rudy, R. J., Venturini, C. C., Mazuk, S., & Puetter, R. C. 2001, *AJ*, **122**, 2013
 Madonna, S., García-Rojas, J., Sterling, N. C., et al. 2017, *MNRAS*, submitted
 Mashburn, A. L., Sterling, N. C., Madonna, S., et al. 2016, *ApJL*, **831**, L3
 Otsuka, M., Kemper, F., Hyung, S., et al. 2013, *ApJ*, **764**, 77
 Otsuka, M., Kemper, F., Leal-Ferreira, M. L., et al. 2016, *MNRAS*, **462**, 12
 Otsuka, M., Meixner, M., Riebel, D., et al. 2011, *ApJ*, **729**, 39
 Péquignot, D., & Baluteau, J. P. 1994, *A&A*, **283**, 593
 Péquignot, D., Morisset, C., & Cassasus, S. 2012, in IAU Symp. 283, Planetary Nebulae: An Eye to the Future, ed. A. Manchado, L. Stanghellini, & D. Schönberner (Cambridge: Cambridge Univ. Press), 470
 Porter, R. L., Ferland, G. J., Storey, P. J., & Detisch, M. J. 2012, *MNRAS*, **425**, L28
 Rudy, R. J., Erwin, P., Rossano, G. S., & Puetter, R. C. 1992, *ApJ*, **384**, 536
 Rudy, R. J., Venturini, C. C., Lynch, D. K., Mazuk, S., & Puetter, R. C. 2002, *ApJ*, **573**, 794
 Sharpee, B., Zhang, Y., Williams, R., et al. 2007, *ApJ*, **659**, 1265
 Simcoe, R. A., Burgasser, A. J., Schechter, P. L., et al. 2013, *PASP*, **125**, 270
 Sterling, N. C. 2011, *A&A*, **533**, A62
 Sterling, N. C., & Dinerstein, H. L. 2008, *ApJS*, **174**, 158
 Sterling, N. C., Dinerstein, H. L., Kaplan, K. F., & Bautista, M. A. 2016, *ApJL*, **819**, L9
 Sterling, N. C., Porter, R. L., & Dinerstein, H. L. 2015, *ApJS*, **218**, 25 (SPD15)
 Sterling, N. C., & Stancil, P. C. 2011, *A&A*, **535**, A117
 Sterling, N. C., & Witthoef, M. C. 2011, *A&A*, **529**, A147
 Tauheed, A., & Hala 2012, *PhysS*, **85**, 025304
 Witthoef, M. C., Badnell, N. R., del Zanna, G., Berrington, K. A., & Pelan, J. C. 2006, *A&A*, **446**, 361
 Zhang, Y., Liu, X.-W., Luo, S.-G., Péquignot, D., & Barlow, M. J. 2005, *A&A*, **442**, 249